RSC Advances

PAPER

View Article Online
View Journal | View Issue

Check for updates

Cite this: *RSC Adv.*, 2019, **9**, 28165

Enhanced hydrogen evolution from water splitting based on ZnO nanosheet/CdS nanoparticle heterostructures†

Yinwei Wang,[a] Hang Ping, *[a] Tiening Tan,[a] Wenxuan Wang,[a] Peiyan Ma[b] and Hao Xie [b]

Received 1st July 2019
Accepted 2nd September 2019

DOI: 10.1039/c9ra04975d

rsc.li/rsc-advances

As environmental and energy problems have worsened worldwide, research for developing renewable energy has become urgent. Presently, the primary focus of such research is directed towards the photocatalytic decomposition of water to produce hydrogen as an energy source. Herein, ZnO nanosheet/CdS nanoparticle heterostructures were synthesized by a mild wet chemical reaction and displayed a high photocatalytic efficiency (1040 μmol g^{-1} h^{-1}) without Pt loading under visible light radiation. The structure was prepared by first constructing two-dimensional nanocrystalline ZnO flowers and then loading CdS nanoparticles onto the nanocrystals. Results show that this structure can facilitate the separation of photogenerated electrons and holes and improve the photocatalytic efficiency and stability of the materials in the photocatalytic decomposition of water. By changing different experimental conditions to prepare a variety of samples and test their properties, we can analyze the optimal parameters for the preparation of this material.

Open Access Article. Published on 06 September 2019. Downloaded on 4/8/2026 1:34:29 AM.
This article is licensed under a Creative Commons Attribution-NonCommercial 3.0 Unported Licence.

Introduction

The detrimental effects of environmental pollution and global warming on living organisms, particularly humans, have become a major concern and require immediate attention. The root of these problems is the indiscriminate emission of greenhouse and harmful gases from the combustion of fossil fuels. Fossil fuels are non-renewable resources, and their excessive consumption will lead to a serious energy crisis. As a new clean and efficient energy source, hydrogen has attracted wide attention because of its high combustion heat and clean combustion products.[1–6] In 1972, Fujishima first achieved hydrogen production through the photocatalytic decomposition of water using a titanium dioxide semi-conductor as an electrode under ultraviolet irradiation.[7] Since then, hydrogen evolution from water splitting based on photocatalytic technology has been widely and deeply studied. Although this technology appears promising to solve global energy and environmental problems, determining and designing optimal semiconductor photocatalysts to efficiently convert solar energy to hydrogen energy remain a significant task.

In a representatively photocatalytic process, semiconductor materials experience roughly three steps: (1) sunlight excites an electron from the conduction band to the valence band and forms a photogenerated electron–hole pair; (2) photo-generated electrons and holes transport or recombine on the surface and in the bulk of a semiconductor, then migrate to the surface of the semiconductor; (3) photogenerated carriers, migrating to the surface of the semiconductor, induce the redox reaction.[8,9] Therefore, the selection of a semiconductor photocatalyst is determined by band gap, structure, stability, among other factors. The band gap width directly determines the efficiency of the photogenerated electron–hole, where a wider band gap requires a higher excitation energy, and most visible light cannot be absorbed effectively. The structure or morphology of the semiconductor greatly affects the absorption efficiency, the carrier transport path or rate of carriers, electron–hole recombination, *etc.* For example, one-dimensional nanostructures can facilitate electron transport and the separation of photogenerated carriers.[10] In the process of photocatalysis, redox reactions on the surface of semiconductors will lead to photocorrosion of the semiconductor; thus, it is very important to enhance photostability of the semiconductor photocatalyst.

Numerous studies have fabricated various semiconductor photocatalysis, including TiO_2, ZnO, C_3N_4, CdS, MoS_2 and graphene/black phosphorus in order to improve the efficiency of hydrogen production.[11–18] ZnO is a common photocatalyst semiconductor with a direct band gap, which can effectively avoid the low electron transition probability in indirect semiconductors, and offers advantages of high

[a]*State Key Laboratory of Advanced Technology for Materials Synthesis and Processing, Wuhan University of Technology, Wuhan 430070, China. E-mail: pinghang0716@163.com*

[b]*School of Chemistry, Chemical Engineering and Life Science, Wuhan University of Technology, Wuhan, 430070, China*

† Electronic supplementary information (ESI) available. See DOI: 10.1039/c9ra04975d

Open Access Article. Published on 06 September 2019. Downloaded on 4/8/2026 1:34:29 AM.
This article is licensed under a Creative Commons Attribution-NonCommercial 3.0 Unported Licence.

photosensitivity, low cost, non-toxic environmental protection, *etc.* However, the wide band gap (3.2 eV) and fast recombination of photogenerated carriers severely inhibit ZnO semiconductors' photocatalytic efficiency.[19–22] While CdS can split water under visible light due to its narrow band gap (2.4 eV), its photocorrosion seriously limits its recycling utilization efficiency as a photocatalyst.[23] Considering the advantages of both materials, CdS has been adopted to sensitize ZnO in many studies. Previous literatures have reported the syntheses of ZnO and CdS heterostructures to form respective hybrid systems, which are used to improve the efficiency of hydrogen production and stability.[24–26] For instance, X. W. Wang *et al.* prepared ZnO/CdS nanocrystalline heterostructures by a wet chemical reaction at 60 °C for 24 h. After loading noble metal Pt, the hydrogen production efficiencies of CdS and ZnO were 14 and 40 times higher than that of single ZnO, respectively.[25] D. D. Ma *et al.* prepared CdS/ZnO heterostructures by coating CdS quantum dots on ZnO nanosheets *via* a hydrothermal method assisted by ultrasound. The hydrogen production efficiency of this material was 22.12 mmol g^{-1} h^{-1}, which is 13 and 138 times higher than that of single ZnO.[3] S. Mukhopadhyay *et al.* prepared disk ZnO by an ultrasonic chemical method, then deposited CdS nanoparticles on the disk surface using a hydrothermal method. The hydrogen production efficiency of the composite was 22 times higher than that of single ZnO in visible light.[26] Although these results of the above works are promising, the synthesis of ZnO/CdS heterostructures requires high temperatures and complex preparation methods, which are energy-consuming procedures.

Herein, we prepared ZnO/CdS heterostructures through a simple synthesis method under low temperatures. The flower-like ZnO was assembled by single-crystal nanosheets with a thickness of 10 nm, followed by the uniform deposition of CdS nanoparticles with a diameter of 5 nm on the surface of the nanosheets. The loading content of CdS can be controlled by incubating different concentrations of ZnO nanosheets in the reaction solution. The 2D nanosheets provide an ideal platform for confining the growth of CdS[27] and facilitate the fast transport of carriers to prohibit the recombination of photogenerated electrons and holes. As expected, the prepared CdS/ZnO heterostructure without Pt loading exhibits the highest hydrogen evolution rate of 1040 μmol g^{-1} h^{-1}, about four times that of solely CdS under visible light irradiation. In addition, the CdS/ZnO heterostructure we prepared also has excellent cycle stability. The results demonstrate that the ZnO nanosheets/CdS nanoparticles heterostructure has good potential as a photocatalyst for hydrogen evolution. The main text of the article should appear here with headings as appropriate.

Experimental section

Chemical reagent

Zinc nitrate [$Zn(NO_3)_2 \cdot 6H_2O$], sodium hydroxide (NaOH), cadmium chloride ($CdCl_2 \cdot 2.5H_2O$), and sodium sulfide ($Na_2S \cdot 9H_2O$) were purchased from Sinopharm Chemical Reagent Co., Ltd. without further purification.

Synthesis of flower-like ZnO

$Zn(NO_3)_2 \cdot 6H_2O$ was selected as the zinc source to prepare a 0.1 M Zn^{2+} solution, into which 1.0 g NaOH solid powder was added. After stirring for 5 min, the mixed solution was placed into a water bath at 40 °C for 6 h. NaOH was used to control the hydration of zinc ions by changing the pH of the solution. The precipitate was centrifuged, washed with deionized water three times, then dried in a lyophilizer (denoted as ZnO@2 : 5) to obtain the powder. In order to explore the effect of NaOH on the morphology of ZnO products, various amounts of NaOH (0.5, 0.6, 0.8, 1.2, and 1.6 g) were added into the Zn^{2+} solution under the same conditions then denoted as ZnO@1 : 5, 1 : 6, 1 : 8, 2 : 6, and 2 : 8, respectively.

Synthesis of ZnO/CdS heterostructures

Flower-like ZnO powders assembled by nanosheets were chosen as the raw material for the preparation of ZnO/CdS composites. 50 mg ZnO powder was poured into a beaker containing 50 ml Cd^{2+} solution. To control the loading content of CdS, we varied the concentration of Cd^{2+} in the solution (200, 120, 100, 50, 20, 12.5, and 10 mM) in a reaction with ZnO for 1 h. The products were centrifuged and washed, then dispersed in 20 ml S^{2-} solution (20 mM), and agitated for 1 h to obtain the final powder. Finally, the reactants were centrifuged, washed, and dried. As the control group, CdS powder was synthesized through mixing 20 mM Cd^{2+} and 20 mM S^{2-} solution.

Characterization

X-ray diffraction (XRD) patterns were obtained using Bruker D8 Advance with Cu Kα radiation (V = 40 kV, I = 40 mA) in the range of 15–75°. Surface morphology information was revealed by field emission scanning electron microscopy (FESEM; Hitachi S-4800) at 5 kV. High resolution transmission electron microscopy (HRTEM) examination was carried out with a JEOL JEM 2100F at 200 kV equipped with an energy-dispersive spectroscopy (EDS) detector. Specific surface area was determined by an ASAP 2020M adsorption apparatus using the Brunauer–Emmet–Teller (BET) method. X-ray photoelectron spectroscopy (XPS) measurements were conducted using a ThermoFisher Escalab 250Xi.

Photocatalytic hydrogen generation

The photocatalytic splitting of water to produce hydrogen occurred in a closed glass flask using a 300 W Xenon lamp (λ > 420 nm) to simulate the solar light source. $Na_2S \cdot 9H_2O$ (0.1 M) and Na_2SO_3 (0.1 M) were dissolved in 80 ml of deionized water and poured into the flask, followed by the addition of 25 mg ZnO/CdS powder. In order to disperse the powder evenly in the solution, the flask was placed in a supersonic instrument for ultrasonic dispersion of 5 min, then the solution was stirred again for 3 to 5 min. After repeating the above operations 3 times, the flask was filled with nitrogen for 15 min to exclude air. The flask was placed in the middle position of a Xenon lamp source (current 10 A, power 300 W, filter: λ > 420 nm), and the speed of magnetic stirring was set to 700 rpm. The spectrum of

 This journal is © The Royal Society of Chemistry 2019

Open Access Article. Published on 06 September 2019. Downloaded on 4/8/2026 1:34:29 AM.
This article is licensed under a Creative Commons Attribution-NonCommercial 3.0 Unported Licence.

filter indicates there is no UV leaking (Fig. S1†). The distance between light source and flask is 15 cm. The temperature of the reactor flask is controlled by air conditioner with constant temperature at 24 °C. Irradiation under the Xenon lamp occurred for 2 h with sampling and testing every half hour. During sampling, the sampler of the gas chromatograph was inserted into the rubber plug of the flask to absorb 0.4 ml gas, which caused the gas to enter the chromatograph quickly, followed by immediate measurement readings.

Results and discussions

The morphology and structure of the ZnO products were observed by SEM and TEM. SEM images show that ZnO powders exhibit a three-dimensional floral structure with an average diameter of 2 m and are assembled by a large amount of flat nanosheets (Fig. 1a–c). The nanosheets exhibit a thickness of about 10 nm (Fig. 1d and e) and a single crystal structure with an interplanar spacing of 0.28 nm, corresponding to the (100) planes of ZnO (Fig. 1e). Fig. 1f shows that the nanosheets are composed of nanorods with the same orientation; the gaps between nanorods are marked by red arrow. During the formation of nanosheets, the nanorods may directionally growth and gradually merge into a perfect nanosheet (Fig. S2†). In order to explore the effect of alkali on the structure of ZnO, various concentrations of NaOH were added into the reaction system (Fig. S3 and S4†). Smooth platelets were observed in ZnO@2 : 6 (1.2 g NaOH), while the needle-like building blocks appeared in ZnO@2 : 8 (1.6 g NaOH), suggesting that higher NaOH content may promote the formation of $Zn(OH)_2$ (Fig. S5†). With the decrease of NaOH content, spherical products were obtained and assembled by close packing nanosheets (Fig. S4†). In addition, the structure of ZnO was broken when the reaction temperature was 50 °C.

To facilitate the deposition of CdS on the surface of ZnO nanosheets, we selected ZnO@2 : 5 with a rigid structure as the experimental sample. After incubating ZnO with Cd^{2+} and S^{2-}, the whole structure was maintained (Fig. 2a and b), and CdS nanoparticles with a 5 nm diameter were observed on ZnO nanosheets (Fig. 2c). In the TEM image, the selected area electron diffraction (SAED) indicates the coexistence of ZnO and

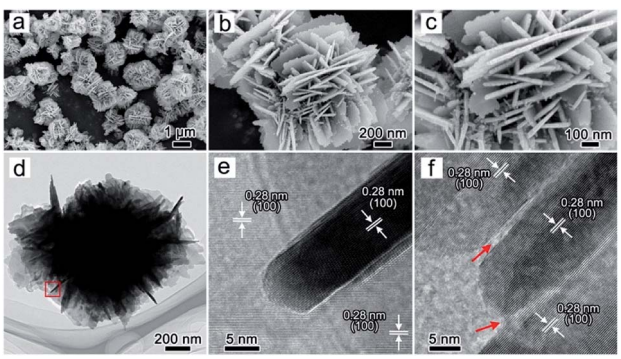

Fig. 1 SEM (a–c) and TEM (d–f) images of the flower-like ZnO (ZnO@2 : 5) incubated at 40 °C for 6 hours.

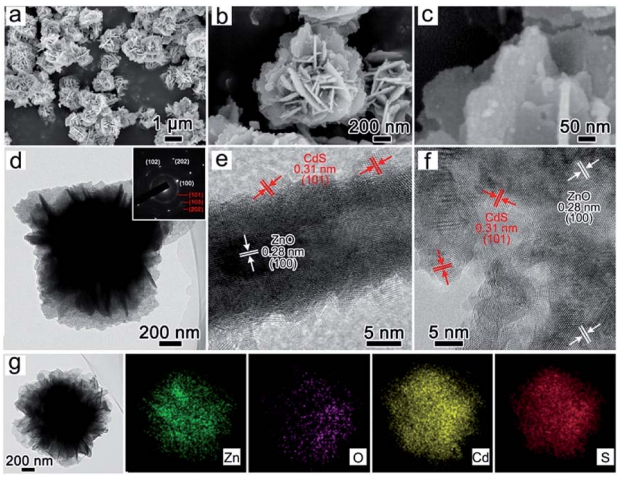

Fig. 2 SEM (a–c) and TEM (d–f) and EDS (g) of the ZnO/CdS heterostructures (the inset in part d is the SAED of the ZnO/CdS composite).

CdS (Fig. 2d and inset). The single crystal-like spots result from the ZnO nanosheets, and the ring diffraction pattern is responded to the random deposition of CdS nanoparticles. The XRD patterns also verify the phase components in the composites (Fig. 3a and S6†). The coating of CdS nanoparticles on ZnO nanosheets is visible from the exterior spaces of the vertical and horizontal nanosheets in Fig. 2e and f. The crystal plane spacing of 0.31 and 0.28 nm is attributed to the exposed crystal plane of CdS (101) and ZnO (100) planes, and the specific surface areas of ZnO@2 : 5 and ZnO/CdS were determined to be

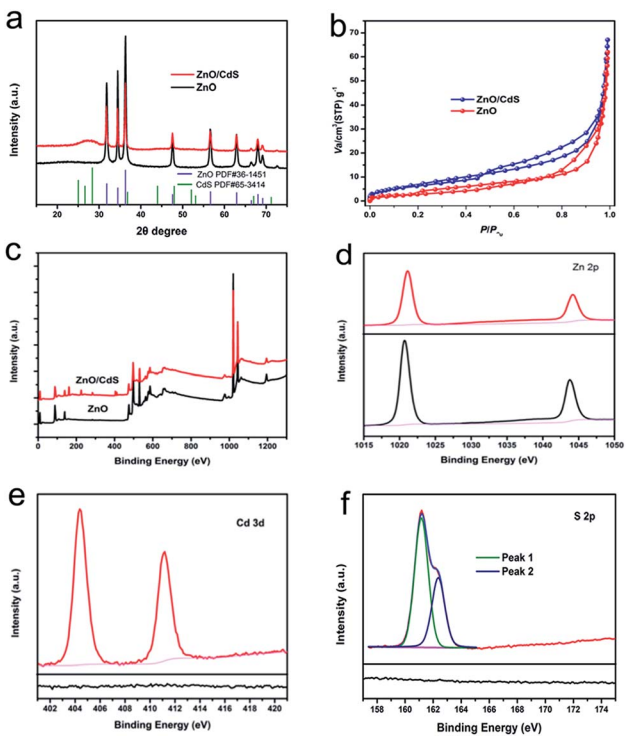

Fig. 3 XRD (a), BET (b) and XPS spectra (c) of ZnO and ZnO/CdS. High resolution XPS spectrum of Zn 2p (d), Cd 3d (e) and S 2p (f).

Open Access Article. Published on 06 September 2019. Downloaded on 4/8/2026 1:34:29 AM.
This article is licensed under a Creative Commons Attribution-NonCommercial 3.0 Unported Licence.

17.2 and 28.4 $m^2 g^{-1}$, respectively. The increase in the specific surface areas of ZnO/CdS may be attributed to the CdS nanoparticles. Fig. 2g and S7† exhibits the uniform distribution of Zn, O, Cd, and S elements in the ZnO/CdS heterostructure. As a control group, the CdS powder with aggregated nanoparticles was individually synthesized through directly mixing Cd^{2+} and S^{2-} (Fig. S8†). The EDS mapping of CdS nanoparticles and ZnO flower was presented in Fig. S9.†

The chemical composition of ZnO/CdS was further analyzed by XPS. Fig. 3c shows the measurement spectra, from which the peaks of elements in sample ZnO and ZnO/CdS can be clearly observed. The high-resolution XPS spectrum of Zn $2p_{3/2}$ and Zn $2p_{1/2}$ shows respective peaks centered at 1021.8 and 1044.9 eV (Fig. 3d), where the spin orbit separation of about 23.1 eV is ascribed to Zn^{2+} in ZnO.[28] Compared with pure ZnO, the weak shift of Zn peaks in ZnO/CdS indicates the chemical bonding between ZnO and CdS. The Cd 3d orbital region (Fig. 3e) reveals the binding energies of Cd $3d_{5/2}$ and Cd $3d_{3/2}$ peaks at 405.1 and 411.8 eV, respectively, where the splitting energy of 6.7 eV is a characteristic value of Cd atoms in CdS. Further, Fig. 3f displays two bonding energy S 2p peaks at 161.5 and 162.5 eV, which are indicative of CdS.

Changing the concentration of Cd^{2+}, we modified the amount of CdS deposited on ZnO. When the concentration ratio of Zn to Cd was 10 : 1, a composite with structural integrity was obtained with visibly apparent CdS nanoparticles (Fig. 4a). Increasing the ratio from 8 : 1 to 2 : 1, the composite with unchanged structure were synthesized, and the loading of CdS in ZnO may increase (Fig. 4b–d). At the same time, the compositions of the samples were not changed through XRD patterns (Fig. 4f and S10†). However, when the ratio was 1 : 1.2, some nanowire-like products appeared on the ZnO nanosheets, meaning the impurity phase was synthesized (Fig. 4e). The impurity phase of $Cd(OH)_2$ was detected in samples with 1 : 2 (Zn : Cd), and the flower-like structure collapsed (Fig. S11†). Since the alkalinity of the S^{2-} solution can cause destruction of the ZnO structure, we changed the load order of S^{2-} (first) and Cd^{2+} (second) on the ZnO nanosheets to prevent this breakage. This resulted in a load effect similar to previous and the structure of the product did not change much (Fig. S12 and S13†). The deposition of CdS on ZnO can also be demonstrated in TEM images (Fig. S14†). To investigate the effect of the formation of ZnO/CdS heterostructure on optical band gap, we tested the UV-vis spectra of pure ZnO and ZnO/CdS 1 : 1 (Fig. S15†). It illustrates that the optical band gap of ZnO/CdS 1 : 1 (2.1 eV) is narrower than pure ZnO (3.1 eV). The band gap of CdS nanoparticle is 2.2 eV (Fig. S16†). The XPS valence spectra of CdS and ZnO are presented in Fig. S17.† The PL spectra of the pure ZnO and ZnO/CdS 1 : 1 which excited at 325 nm is showed in Fig. S18,† it is obviously that compared with pure ZnO, the peak of ZnO/CdS 1 : 1 has a red shift of 25 nm.

The photocatalytic capability of splitting water over these samples was measured under irradiation of 420 nm using the Xenon lamp and Na_2S and Na_2SO_3 as sacrificial agents. It can be

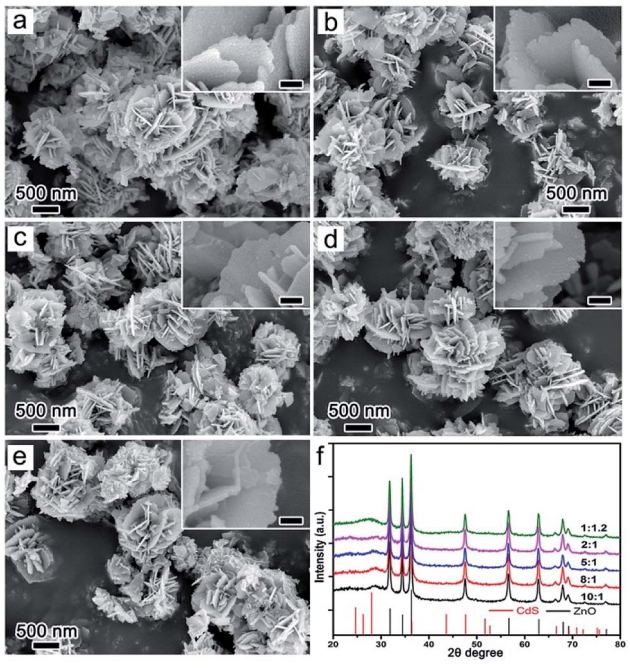

Fig. 4 SEM (a–e) and XRD (f) of the products at different reaction concentration ratio of S and Cd ((a) 10 : 1, (b) 8 : 1, (c) 5 : 1, (d) 2 : 1, (e) 1 : 1.2).

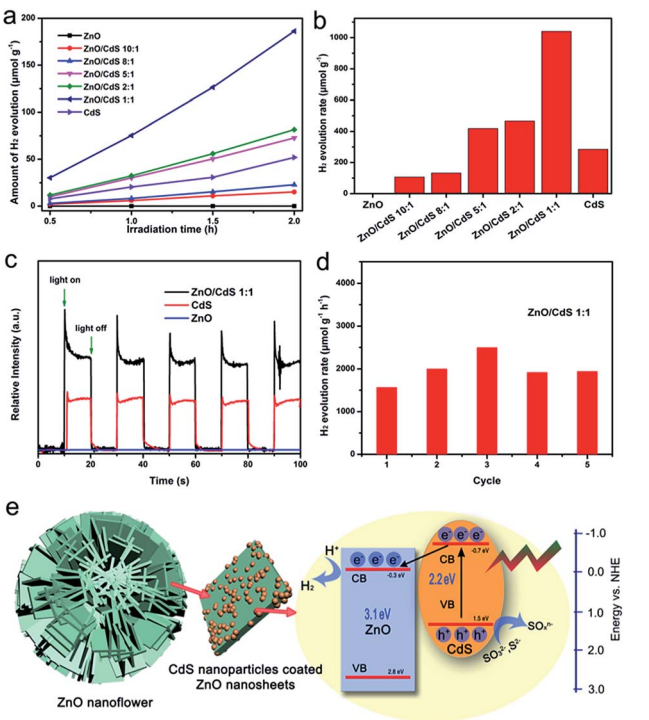

Fig. 5 Comparison of the hydrogen production at different time points (a) and the photocatalytic hydrogen evolution rate (b) over different samples during 2 h; (c) is the photocurrent responses under visible-light (λ > 420 nm) irradiation; (d) is the cycling runs of the ZnO/CdS (1 : 1) photocatalyst, each cycle takes two hours; (e) is the ZnO/CdS heterostructures' photo-catalytic hydrogen production mechanism.

This journal is © The Royal Society of Chemistry 2019

Open Access Article. Published on 06 September 2019. Downloaded on 4/8/2026 1:34:29 AM.
This article is licensed under a Creative Commons Attribution-NonCommercial 3.0 Unported Licence.

seen in Fig. 5a and b that pure ZnO produced almost no hydrogen due to its wide band gap, which prevents excitation of ZnO to produce photogenerated electron and holes under visible light. As the loading of CdS in the ZnO/CdS heterostructure increased, hydrogen production and the hydrogen production rate of the samples (ZnO : CdS) increased to 106.7 (10 : 1), 132.3 (8 : 1), 418.4 (5 : 1), 465.7 (2 : 1), 1040.5 (1 : 1), and 284.6 (CdS) mol g^{-1} h^{-1}. For 5 : 1 (ZnO : CdS), the amount of hydrogen produced and the rate of hydrogen production exceeded that of CdS without ZnO. In the Fig. 5c, it shows the photocurrent response of different photocatalysts. Compared with the pure ZnO and CdS, the ZnO/CdS photocatalysts (1 : 1) we prepared here shows higher photo-current response, demonstrating that the separation between photogenerated electrons and holes in this prepared ZnO/CdS heterostructure is more efficient, which is significant to improve the photocatalytic activity. Meanwhile, the photocurrent of ZnO/CdS 2 : 1/5 : 1/8 : 1/10 : 1 was presented in Fig. S19.† According to the relative intensity of photocurrent, it is confirmed that the content of CdS in ZnO/CdS is proportional to the photocurrent. In order to verify the stability of the ZnO/CdS heterostructure (1 : 1), we also take the recycling photocatalytic performance under the same conditions (Fig. 5d). From the data, it can be seen that the H_2-production rate of the ZnO/CdS (1 : 1) sample within five cycles in 10 hours is relatively stable. Fig. 5e shows the photocatalytic hydrogen production mechanism of ZnO/CdS heterojunction where the CdS nanoparticles loaded on the ZnO nanosheets formed a heterojunction, which is further described as follows. According to the band gap from UV-vis absorption spectra and XPS valence spectra, the alignment modelling was presented. Under illumination, the semiconductor CdS absorbs visible light energy and excites the electron to transition from the valence band to the conduction band and form photogenerated electron–hole pairs. Then, the photogenerated electrons in the CdS conduction band migrate to the conduction band of ZnO through the heterojunction, which inhibits the combination of photogenerated electrons and holes. Photogenerated carriers migrated to the surface of ZnO to produce hydrogen and hole oxidation of S^{2-} and SO_3^{2-} on CdS. Therefore, the ZnO/CdS heterostructure exhibits better photocatalytic capability than pure CdS.

Conclusions

In summary, we propose a low temperature and simple synthesis method to fabricate a ZnO/CdS heterostructure based on flower-like ZnO assembled by nanosheets. By continuously combining Cd^{2+} and S^{2-}, CdS nanoparticles were deposited on ZnO nanosheets. However, when the ratio of Zn : Cd was higher than 1 : 1, the structure of the products could not be maintained, and the ZnO nano-flower structure with nanosheets was broken. Results suggest that the photo-catalytic efficiency of the prepared ZnO/CdS composites is much higher than those of pure ZnO and CdS and depends on the loading content of CdS. It was also found that with the increase in the loading amount of CdS, hydrogen production is enhanced. When ZnO : CdS was in a 1 : 1 ratio, its hydrogen production rate reached 1040.5 μmol g^{-1} h^{-1} without Pt loading. Overall, this work may provide a green and efficient approach to construct the heterostructures for solar-to-fuel conversion and serve as a motivational basis to explore other photocatalysts in hydrogen production.

Conflicts of interest

The authors declare no competing financial interest.

Acknowledgements

This work was funded by the National College Students Innovation and Entrepreneurship Training Program (201810497026). We are grateful to Miss Bi-Chao Xu of the Core Facility and Technical Support, Wuhan Institute of Virology for her technical support in sample preparation. The authors declare that they have no conflict of interest.

Notes and references

1 J. Low, J. Yu, M. Jaroniec, S. Wageh and A. A. Al-Ghamdi, *Adv. Mater.*, 2017, 1601694.
2 N. Chouhan, R. Ameta, R. K. Meena, N. Mandawat and R. Ghildiyal, *Int. J. Hydrogen Energy*, 2016, **41**, 2298–2306.
3 D. Ma, J. W. Shi, Y. Zou, Z. Fan, X. Ji and C. Niu, *ACS Appl. Mater. Interfaces*, 2017, **9**, 25377–25386.
4 D. Ma, J. W. Shi, Y. Zou, Z. Fan, X. Ji, C. Niu and L. Wang, *Nano Energy*, 2017, **39**, 183–191.
5 J. X. Lv, Z. M. Zhang, J. Wang, X. L. Lu, W. Zhang and T. B. Lu, *ACS Appl. Mater. Interfaces*, 2019, **11**, 2655–2661.
6 J. K. Vaishnav, S. S. Arbuj, S. B. Rane and D. P. Amalnerkar, *RSC Adv.*, 2014, **4**, 47637–47642.
7 A. Fujishima and K. Honda, *Nature*, 1972, **238**, 37–38.
8 S. R. Lingampalli, U. K. Gautam and C. N. R. Rao, *Energy Environ. Sci.*, 2013, **6**, 3589–3594.
9 P. Zhou, J. G. Yu and M. Jaroniec, *Adv. Mater.*, 2014, **26**, 4920–4935.
10 G. R. Yang, W. Yan, Q. Zhang, S. H. Shen and S. J. Ding, *Nanoscale*, 2013, **5**, 12432–12439.
11 J. Jin, C. Wang, X. N. Ren, S. Z. Huang, M. Wu, L. H. Chen, T. Hasan, B. J. Wang, Y. Li and B. L. Su, *Nano Energy*, 2017, **38**, 118–126.
12 G. Lia, Z. Lian, W. Wang, D. Zhang and H. Li, *Nano Energy*, 2016, **19**, 446–454.
13 H. Moa, C. Song, Y. Zhou, B. Zhang and D. Wang, *Appl. Catal., B*, 2018, **221**, 565–573.
14 W. Liu, X. Wang, H. Yu and J. Yu, *ACS Sustainable Chem. Eng.*, 2018, **6**, 12436–12445.
15 X. Wang, Q. Li, P. Shi, J. Fan, Y. Min and Q. Xu, *Small*, 2019, **15**, 1901530.
16 S. Gong, Z. Jiang, P. Shi, J. Fan, Q. Xu and Y. Min, *Appl. Catal., B*, 2018, **238**, 318–327.
17 T. Wu, Y. Ma, Z. Qu, J. Fan, Q. Li, P. Shi, Q. Xu and Y. Min, *ACS Appl. Mater. Interfaces*, 2019, **11**, 5136–5145.
18 K. Liao, S. Chen, H. Wei, J. Fan, Q. Xu and Y. Min, *J. Mater. Chem. A*, 2018, **6**, 23062–23070.

Open Access Article. Published on 06 September 2019. Downloaded on 4/8/2026 1:34:29 AM.
This article is licensed under a Creative Commons Attribution-NonCommercial 3.0 Unported Licence.

19 S. G. Kumar and K. S. R. Koteswara Rao, *RSC Adv.*, 2015, **5**, 3306–3351.
20 S. Cho, J.-W. Jang, J. S. Lee and K.-H. Lee, *Langmuir*, 2010, **26**, 14255–14262.
21 R. Lv, T. Wang, F. L. Su, P. Zhang, C. J. Li and J. L. Gong, *Nano Energy*, 2014, **7**, 143–150.
22 S. Khanchandani, S. Kundu, A. Patra and A. K. Ganguli, *J. Phys. Chem. C*, 2012, **116**, 23653–23662.
23 S. Tso, W. S. Li, B. H. Wu and L. J. Chen, *Nano Energy*, 2018, **43**, 270–277.
24 C. Baslak, E. Aslan, I. H. Patir, M. Kus and M. Ersoz, *Int. J. Hydrogen Energy*, 2016, **41**, 20523–20528.
25 X. W. Wang, G. Liu, Z. G. Chen, F. Li, L. Z. Wang, G. Q. Lu and H. M. Cheng, *Chem. Commun.*, 2009, 3452–3454.
26 S. Mukhopadhyay, I. Mondal, U. Pal and P. S. Devi, *Phys. Chem. Chem. Phys.*, 2015, **17**, 20407–20415.
27 H. Ping, H. Xie and Z. Fu, *Journal of Materiomics*, 2017, **3**, 83–95.
28 G. Yang, W. Yan, Q. Zhang, S. Shen and S. Ding, *Nanoscale*, 2013, **5**, 12432–12439.

This journal is © The Royal Society of Chemistry 2019